Progress In Electromagnetics Research M, Vol. 110, 11–24, 2022

Design of the Outer-Rotor Coreless Bearingless Permanent Magnet Synchronous Generator Based on an Improved MOPSO Algorithm

Junqi Huan and Huangqiu Zhu*

Abstract—The study of outer-rotor coreless bearingless permanent magnet synchronous generator (ORC-BPMSG) is intended to pave the way for the future of high-speed flywheel energy storage systems. A multi-objective parameter optimization method is proposed for the outer-rotor coreless bearingless permanent magnet synchronous generator with the aim of improving the fundamental wave content of the generator's output voltage, reducing harmonics, and optimizing the suspension force at the same time. Firstly, the basic parameters and operating principle of the generator are described. Then, the response surface (RS) method is used to obtain the objective functions for the total harmonics distortion (THD), the mean value of the suspension force and suspension force pulsation. The optimal optimizations of the ORC-BPMSG are selected by establishing the pareto solution set through the improved multi-objective particle swarm optimization (MOPSO) algorithm. Finally, the optimal ORC-BPMSG prototype is fabricated, and the performance of the prototype is verified. The experiments show that the optimized generator output voltage has fewer harmonics and operates reliably.

1. INTRODUCTION

Flywheel energy storage is a promising physical energy storage technology with the advantages of high storage density, high instantaneous power, short charging time, easy measurement of charging and discharging degree, long service life, and no harm to the environment [1–3]. When flywheel energy storage is moving toward higher rotational speed and higher energy storage density, the addition of magnetic suspension bearings reduces the friction between flywheel rotor and bearings and decreases the loss. For the core of flywheel energy storage, high-speed motors, the advantages of zero friction, zero loss, zero pollution, high speed, high precision, and long life can be achieved by using bearingless motor technology to improve the performance of the whole flywheel energy storage system [4–7]. However, the conventional bearingless motor operates at high speed because of the mutual attraction of the stator core and permanent magnet magnets, which generates a large cogging torque, increases the torque pulsation, and improves the difficulty of motor suspension [8–10]. A coreless bearingless permanent magnet synchronous motor/generator is thus proposed [11, 12]. ORC-BPMSG has no mechanical loss, No. cogging torque, and light weight, while the outer rotor design facilitates heat dissipation and increases rotational inertia. ORC-BPMSG becomes a very ideal choice for generators for flywheel energy storage.

The research on the prototype design of coreless bearingless permanent magnet synchronous motor/generator is still in the initial stage, but the optimized design of general permanent magnet synchronous motor/generator is still of reference significance. The research on the optimal design of the prototype of ORC-BPMSG is still blank. There have been many studies for the optimal design of permanent magnet synchronous generators. In [13], an approximate solution based on the mathematical

Received 22 February 2022, Accepted 24 March 2022, Scheduled 18 April 2022
* Corresponding author: Huangqiu Zhu (zhuhuangqiu@ujs.edu.cn).
The authors are with the School of Electrical and Information Engineering, Jiangsu University, Zhenjiang 212013, China.

model of the motor to solve the air gap and permanent magnet thickness is investigated to design a high-efficiency surface permanent magnet synchronous generator by means of an empirical design formula for the motor and finite element analysis. The coreless and bearingless permanent magnet synchronous generator lacks empirical formulas, and the conventional design methods cannot design the parameters well and quickly. In [14–16], the optimization method for the iron-coreless motor is chosen to optimize a single parameter, ignoring the effect of that parameter on other motor performance indexes. The multi-objective parameter optimization method is a method that optimizes multiple objectives and synergizes multiple parameters and is well suited for the optimal design of the ORC-BPMSG. In [17–19], Taguchi's method is used to optimize multiple objectives, but the accuracy of Taguchi's method is not high, and the experimental data are few, which limits the optimization effect to some extent. In [20], a multi-objective optimization method combining Taguchi method and response surface method improves the shortcomings of Taguchi method, but the method is more complicated and time-consuming. In [21], a multi-objective genetic particle swarm optimization algorithm is proposed and applied to the optimal design of bearingless switched reluctance motors with short consumption time and high optimization efficiency. The use of intelligent algorithms to optimize the design of motors has become a simple and reliable design idea with good optimization results.

A multi-objective optimization method combining response surface method and modified multi-objective optimization particle swarm algorithm (MOPSO) is proposed to be applied to ORC-BPMSG in this paper. In Section 2, the basic structure and working principle are introduced. In Section 3, the multi-objective optimization design of the ORC-BPMSG is carried out, detailing the selection of objectives and factors, and the application of response surface and improved MOPSO. In Section 4, the simulation results of the finite element model with optimal parameters are analyzed. In Section 5, the experimental procedure and experimental results are presented to verify the theory. Conclusions are drawn in Section 6.

2. BASIC STRUCTURE AND WORKING PRINCIPLE OF THE ORC-BPMSG

2.1. Basic Structure of the ORC-BPMSG

The ORC-BPMSG consists of a coreless stator, tile-shaped permanent magnets, suspension force windings, power generation windings, and an outer rotor. Compared with conventional permanent magnet synchronous motors, the stator of ORC-BPMSG is casted from epoxy resin material, which greatly reduces the weight of the motor. Applying the ORC-BPMSG to flywheel energy storage provides greater rotational inertia than an inner-rotor generator and allows more weight to be allocated to the flywheel, allowing more energy to be stored. the ORC-BPMSG also compresses the length of the flywheel system axially, allowing for a more compact structure. Since the stator does not have a core, the generator operates without cogging torque, so the quality of the suspension force generated by the suspension force winding is improved, and it is easier to ensure stable rotor suspension. The stator is made of non-epoxy resin material, which not only is non-conductive but also has high mechanical properties. The stator is a 36-slot structure, because it is a nonpermeable material, and the slot type is a common pear-shaped slot. The permanent magnet with pole pair number 3 is attached to the inner surface of the outer rotor, and the outer rotor is made of conventional 0.5 mm silicon steel sheet laminated. The power generation winding and suspension force winding are concentrically wound on the stator slot with a pole pair number of 3 for the power winding and a pole pair number of 2 for the suspension force winding. The winding on the side of the outer rotor is the power generation winding for generating the induced voltage, and the winding away from the outer rotor is the suspension force winding for generating the suspension force.

2.2. Principle of Suspension Force Generation

In the air gap space of a motor, if the magnetic field is not centrosymmetric, then the Maxwell forces on the rotor are also not centrosymmetric. In order to suspend the rotor, a controlled unbalanced magnetic field must be generated in the air gap space of the motor. The ORC-BPMSG, like conventional bearingless motors, has two sets of windings embedded in the stator, one for generating electricity and one for generating suspension force. The two sets of windings satisfy a relationship of 1 difference in

the number of pole pairs, which is one of the conditions for a bearingless motor to be able to suspend stably. The ORC-BPMSG proposed in this paper has a generation winding with the pole-pair number $P_G = 3$ and a suspension force winding with the pole-pair number $P_B = 2$, which satisfies the condition that the pole-pair numbers differ by 1. Figure 1 shows the radial suspension force mechanism analysis diagram of the ORC-BPMSG, where NG is the generation winding, and N_S is the suspension force winding. When both windings are fed with alternating currents of the same frequency, each produces a corresponding magnetic chain, and the chains at air gap 1 superimpose on each other and cancel with each other at air gap 2. According to Maxwell's tensor method, the rotor surface is subjected to a radial suspension force in the positive direction along the y-axis, and by the same token, a suspension force in the opposite direction can be obtained by passing a reverse current through the suspension force winding N_S. Thus, the suspension force can be generated in any direction by varying the current.

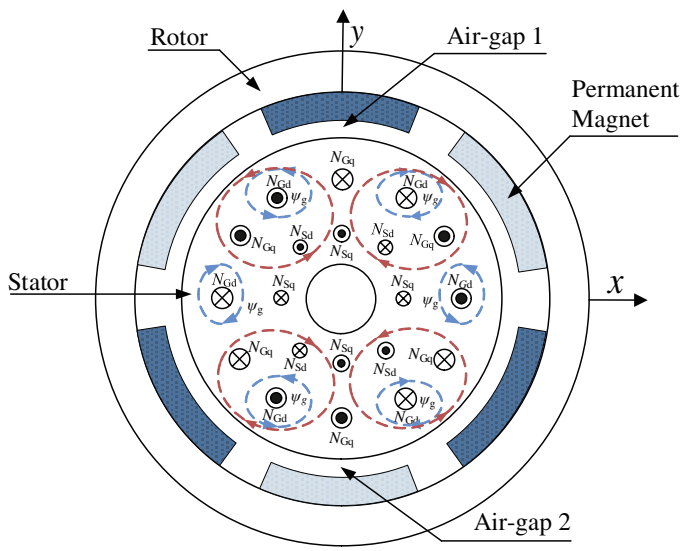

Figure 1. Suspension force generation mechanism.

3. OPTIMIZED DESIGN OF THE ORC-BOMSG

3.1. Selection of the Optimization Objectives

The performance testing indexes of conventional generators are mainly voltage regulation rate and harmonic distortion rate, while the performance of the suspension force of the ORC-BPMSG also needs to be considered in the design process. In order to improve the carrying performance of the ORC-BPMSG, reduce harmonics, increase the magnitude of the suspension force, and reduce the pulsation of the suspension force, this paper proposes a multi-objective optimization design method based on response surface and improved MOPSO. The optimization process of this method is shown in Figure 2.

The initial parameters of the ORC-BPMSG proposed in this paper are shown in Table 1.

Finite element simulations are carried out for the initial prototype parameters, and the initial prototype no-load EMF waveform and EMF waveform are shown in Figure 3(a) when the load is three $500\,\Omega$ resistors connected in a star shape. The voltage regulation rate ΔU is calculated as

$$\Delta U = \frac{U_0 - U}{U_0} \times 100\% \tag{1}$$

where U_0 is the no-load voltage, and U is the load voltage.

From the RMS value substitution can be calculated to get the voltage adjustment rate of 0.44%, which is much less than 5%. The voltage regulation is small because the internal resistance of this generator is very small, and the current variation produces a small voltage drop. So optimization of the voltage regulation rate is not considered.

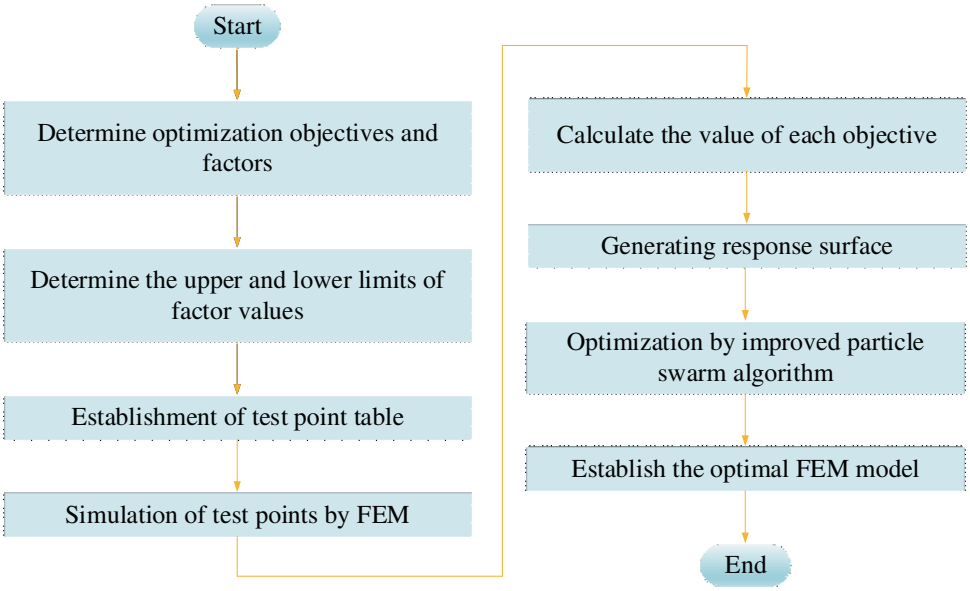

Figure 2. Process of optimization.

Table 1. Main parameters of the ORC-BPMSG.

Parameter	Value
Output power	3 kW
Rated speed	8 00 rpm
Slots	36
Rotor outer diameter	170 mm
Rotor inner diameter	136 mm
Stator outer diameter	116 mm
Air gap length	2 mm
Permanent magnet thickness	8 mm
Polepair number of generation windings	3
Polepair number of suspension force windings	2
Pole-arc coefficient	0.8

The fast Fourier transform of the band-loaded counter-electromotive force waveform is shown in Figure 3(b), and the total harmonic distortion rate is calculated from Eq. (2).

$$THD = \frac{\sqrt{U_2^2 + U_3^2 + \ldots + U_n^2}}{U_1} \times 100\% \tag{2}$$

where U_n is the effective value of nth harmonic, and U_1 is the effective value of the fundamental wave.

The total harmonic distortion rate of the initial prototype is obtained as 19.8%.

The outer rotor is subjected to a suspension force as shown in Figure 3(c), and the suspension force pulsation F_{ripple} is defined as the ratio of the peak-to-peak and average suspension force, whose expression is:

$$F_{\text{ripple}} = \frac{F_{\max} - F_{\min}}{F_{\text{avg}}} \times 100\% \tag{3}$$

After calculation, F_{avg} is 288 N, and F_{ripple} is 3.3%. Because the voltage regulation rate better meets the performance index in the four objectives, the harmonic distortion rate, average suspension

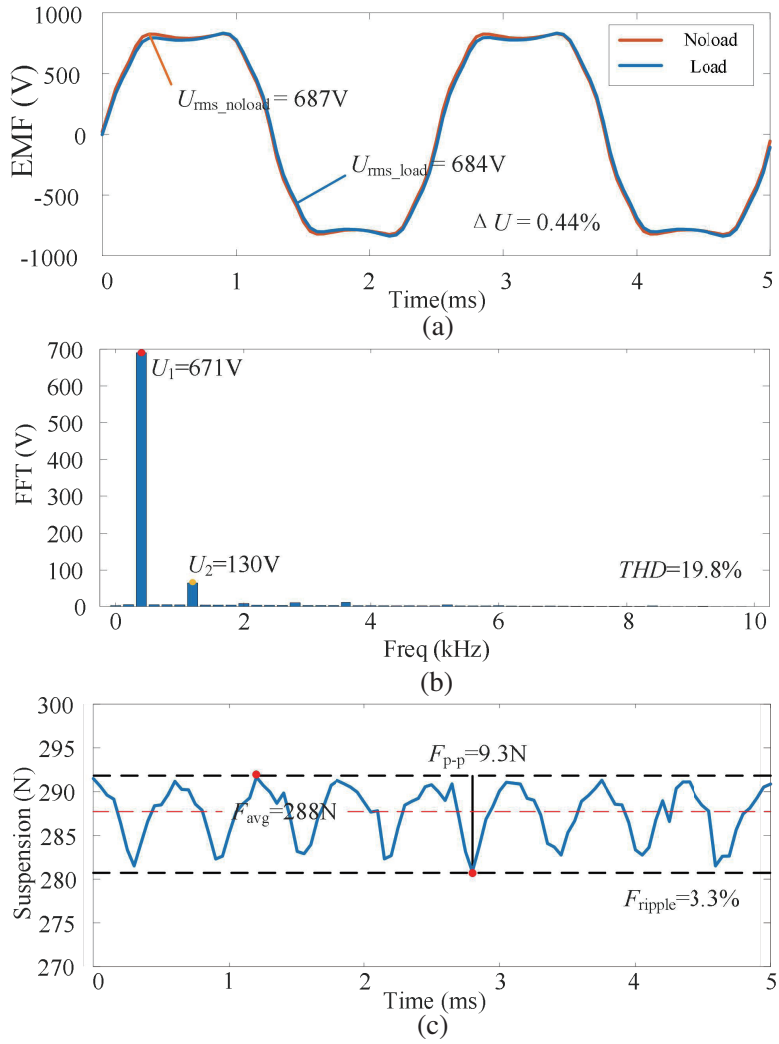

Figure 3. (a) No. load and load EMF waveform. (b) FFT frequency spectrum of EMF. (c) Suspension force waveform.

force, and suspension force ripple are preferentially selected as the optimization objectives for response surface analysis.

3.2. Design Factor Selection and Response Surface Modelling

The ORC-BPMSG uses epoxy resin material for the stator, so changes in the dimensions of the stator slot pattern do not affect the performance of the generator, and the number of design factors available is much reduced. In this paper, the pole-arc coefficient, permanent magnet thickness, air gap length, and outer rotor thickness are selected as design factors as shown in Figure 4.

The response surface method is a statistical method, which uses reasonable tests to obtain certain data, uses a multiple quadratic regression equation to fit a functional relationship between the factors and the response values, and seeks the optimum parameters through analysis of the regression equation. For situations where there are fewer factors and objectives, the Box-Behnken design method is more economical than the central composite design method as it does not require multiple consecutive tests and has a smaller number of test combinations.

Table 2 gives the upper and lower limits for the values of the pole-arc coefficient α, permanent magnet thickness d, air gap length δ, and outer rotor thickness L. According to the Box-Behnken

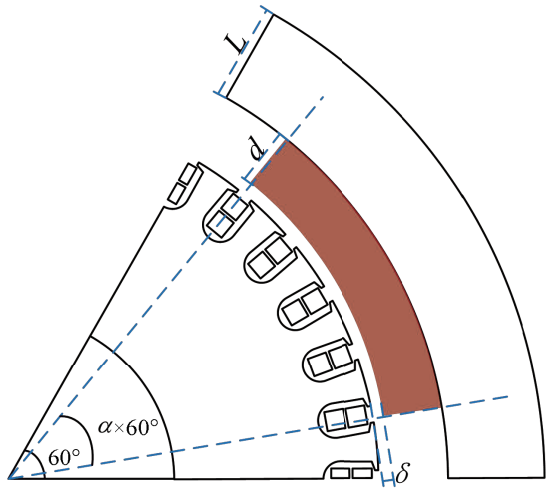

Figure 4. Schematic diagram of design factors in 1/6 models.

Table 2. Levels of design factors.

Level	−1	0	+1
α	0.7	0.85	1
d (mm)	7	8	9
δ (mm)	1	1.5	2
L (mm)	15	17.5	20

method Eq. (4), 29 sets of tests are required for the four factors.

$$N = 2k \times (k-1) + C_0 \tag{4}$$

where k denotes the number of factors, and c_0 denotes the number of repetitions of the central test point, often taking a value of 5 under the four factors, used to estimate the test error, but the same test points in the simulation, to obtain the same calculated results, in fact a total of 25 trials.

The test method uses finite element simulation, where the test points, i.e., combinations of different values of the four factors, are substituted into the ORC-BPMSG model modelled parametrically in advance, and the simulation yields the values of each objective under each test point. The calculated data (29 sets) for the four factors and three objectives are then used with Design Expert Software to generate the response surfaces for each objective and factor as shown in Figure 5.

A fit function for each response surface is also obtained, which can be used to predict a specific level of response for each of the factors. The following equation simplifies the coefficients and removes the terms with weak effects:

$$\begin{cases} THD = -230.6 + 539.9 \times \alpha + 2.1 \times d - 4.3 \times \alpha \times d \\ \qquad - 4.1 \times \alpha \times \delta + 0.1 \times d \times \delta - 264.5 \times \alpha^2 \\ \qquad + 0.2 \times \delta^2 \\ F_{\text{ripple}} = -13.0 + 23.2 \times \alpha + 0.7 \times d - 0.7 \times \delta + 0.4 \times L \\ \qquad - 0.1 \times \alpha \times d - 5.1 \times \alpha \times \delta - 7.3 \times \alpha^2 \\ \qquad - 0.1 \times d^2 + 1.2 \times \delta \\ F_{\text{avg}} = -316.2 + 759.3 \times \alpha + 45.0 \times d - 3.5 \times \delta + 0.2 \times L \\ \qquad + 1.5 \times \alpha \times d - 3.8 \times \alpha \times \delta - 1.0 \times d \times \delta - 410.3 \times \alpha^2 \\ \qquad - 1.2 \times d^2 + 0.5 \times \delta^2 \end{cases} \tag{5}$$

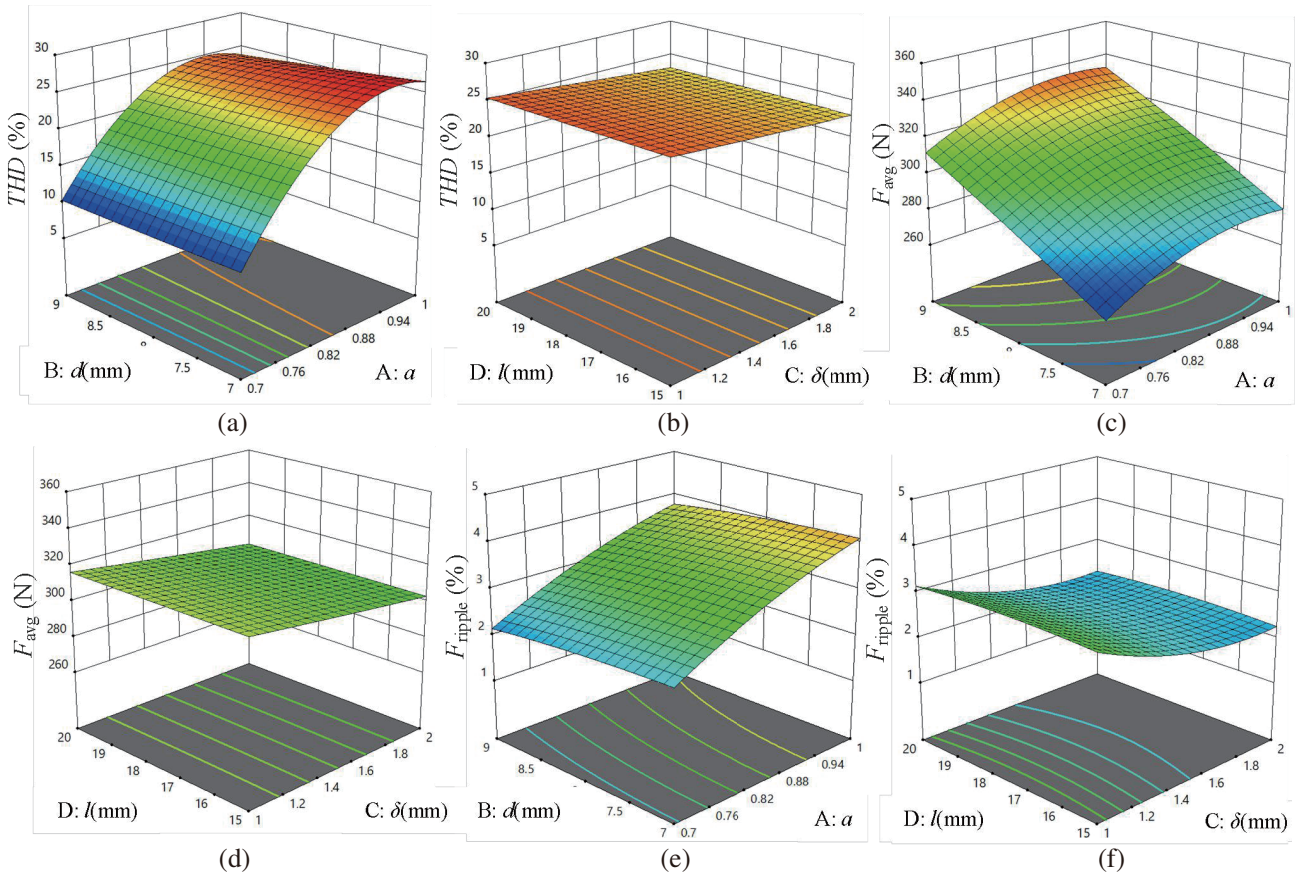

Figure 5. Response surface of each objective.

R^2 is an important measure of the error between the response surface model and the actual model and is known as the coefficient of determination, calculated as shown in Eq. (6):

$$R^2 = \frac{\sum (\hat{y} - \bar{y})^2}{\sum (y - \bar{y})^2} \tag{6}$$

where $\hat{y}$ is the value calculated according to Eq. (5), $\bar{y}$ the average of the 29 sets of objectives, and y the actual value of the objective.

The closer the value of R^2 is to 1, the more accurate the model is. The R^2 for each of the three models is greater than 0.95, satisfying the optimization premise. As can be seen from Figure 5, the $[\alpha\ d\ \delta\ L]$ at the better point of each model takes different values. Therefore, this paper uses the particle swarm optimization algorithm with a view to obtain the pareto optimal solution set for the three objective functions and further selecting the optimal solution that best fits the optimization objective.

3.3. Optimization Based on Improved MOPSO

MOPSO is a population-based intelligent optimization algorithm proposed based on the idea of imitating the foraging behavior of a flock of birds. Assuming that the problem is in D-dimensional space, the velocity vector and position vector are defined as:

$$\begin{cases} V_i = (V_{i1}, V_{i2}, \ldots, V_{id}) \\ X_i = (X_{i1}, X_{i2}, \ldots, X_{id}) \end{cases} \tag{7}$$

Then the update equations of velocity and position can be expressed as:

$$\begin{cases} V_{id}(t+1) = \varphi V_{id}(t) + c_1 \times rand_1()(pBest_{id}(t) - X_{id}(t)) + c_2 \times rand_2()(gBest_d(t) - X_{id}(t)) \\ X_{id}(t+1) = X_{id}(t) + V_{id}(t+1) \end{cases} \tag{8}$$

where φ is the inertia weight coefficient; c_1 and c_2 are acceleration coefficients; and $rand_1$ and $rand_2$ are two random numbers generated within [0, 1], respectively. $pBest_{id}$ represents the best position found by the ith particle so far; $gBest_d$ is the best position found in the whole population; and t represents the number of current iterations.

When the particles of ordinary MOPSO converge too fast, they will shrink toward the local optimum within a few generations, a phenomenon that leads to similar search behaviors among individuals and the loss of population diversity. In this paper, we propose an improved velocity update equation with linear decreasing inertia weights and adaptive detection vectors

$$\begin{cases} V_{id}(t+1) = \varphi V_{id}(t) + c_1 \times rand_1()(pBest_{id}(t) - X_{id}(t)) + c_2 \times rand_2()(gBest_d(t) - X_{id}(t)) \\ \qquad\qquad + c_3 \times rand_3()(R(t) - X_{id}(t)) \\ \varphi = \varphi_{\max} - \dfrac{\varphi_{\max} - \varphi_{\min}}{T} \cdot t \\ R(t) = \dfrac{x^d_{\max} + x^d_{\min}}{2} + \dfrac{x^d_{\max} - x^d_{\min}}{2} \cdot e^{-2t} \cdot \cos(2\pi u) \end{cases} \tag{9}$$

where $\varphi_{\max}$ is the maximum inertia weight, which takes the value of 0.9; $\varphi_{\min}$ is the minimum inertia weight, which takes the value of 0.2; T is the maximum number of iterations; u is a random number in [0,1]; and $x^d_{\max}$ and $x^d_{\min}$ are the upper and lower bounds of the problem, respectively.

A new detection vector $(R(t) - X_{id}(t)$ is added to enable the particles to cover a larger range of solution space with a larger probability using an adaptive variable detection radius $R(t)$. The velocity update equation of the algorithm shows that the population members can explore the unvisited regions in the solution space with a larger probability. A large detection radius facilitates enhanced exploration behavior of the particles by moving them away from the current region and driving them to search for other regions. A small detection radius enhances the exploitation of the best solution of the particle by an adequate search of a small area near this best solution. A large inertia weight is given at the beginning of the iteration, which gradually decreases as the search proceeds. This ensures that the algorithm has a large speed step at the beginning of the search in order to detect a better region at the global scale and to be able to do a refined search around the extremes at a later stage.The improved MOPSO is less prone to fall into local optimal solutions and has higher convergence accuracy and diversity compared to the traditional MOPSO.

After 200 iterations, the non-dominated solution set, i.e., the pareto solution set, is obtained, as shown in Figure 6. It can be seen from Figure 6 that the best choice is at the corner of the curve in

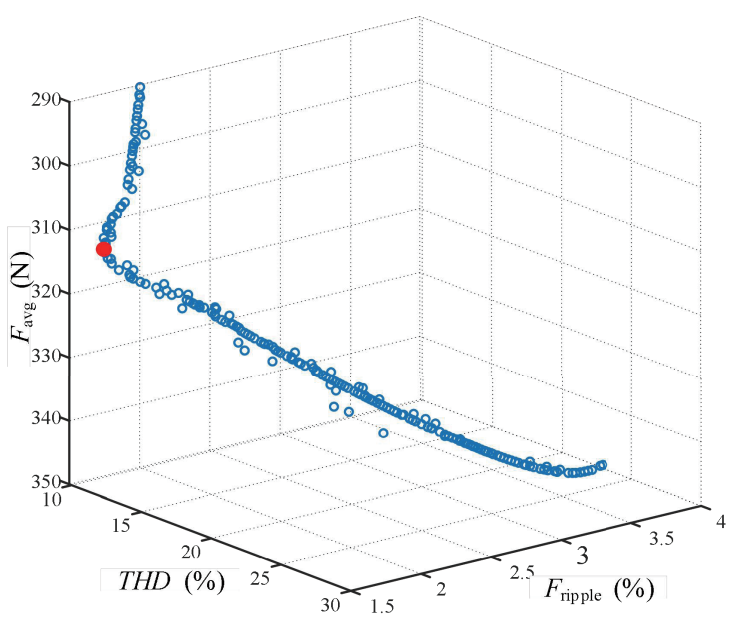

Figure 6. Pareto solution set.

order to obtain the optimal *THD* and suspension force harmonic level, while the suspension force size at the corner is greater than 300 N, which is the very ideal value to take. There are various combinations of $[\alpha\, d\, \delta\, L]$ to choose from near the red dot in Figure 6. The nearby points are listed in order to choose the combination with parameters that are easier to manufacture and use less material, while obtaining the same optimization effect. Obviously, the combination of serial number 6 [0.7 9 1.4 15] in Table 3 shows a small thickness of the outer rotor, which not only reduces the mass, but also has a lower cost, while the length of the air gap is within a reasonable range, so the final optimized parameters are shown in Table 4 and compared with the initial parameters.

Table 3. Levels of design factors.

	α	d (mm)	δ (mm)	L (mm)	*THD* (%)	F_{avg} (N)	F_{ripple} (%)
1	0.7	8.8	2	15.2	9.847	304.2	1.95
2	0.7	8.9	2	15	9.850	305.2	1.93
3	0.7	9	1.7	20	10.343	312.3	1.69
4	0.7	9	1.6	20	10.385	312.7	1.69
5	0.7	9	1.6	20	10.423	313.0	1.68
6	0.7	9	1.4	15	10.690	315.3	1.72
7	0.7	9	1	18	11.431	321.6	2.15

Table 4. Final optimized factor combinations.

Factors	Initial value	Optimized value
α	0.8	0.7
d/mm	8	9
δ/mm	2	1.4
L/mm	17	15

4. RESULTS ANALYSIS

In order to verify that the optimized parameters are effective, finite element simulations are performed for the ORC-BPMSG model with the new key parameters, and then compared with the finite element simulation results of the initial prototype model.

Figure 7(a) shows the force on the outer rotor of the initial prototype and the optimal ORCBPMSG model. It can be seen that the suspension force F_{avg} is increased by 22%, which is greater than 300 N. The suspension force pulsation F_{ripple} is calculated and obtained. The suspension force pulsation is reduced from 3.3% to 1.8%, and the suspension force pulsation F_{ripple} is reduced by 45% after optimization compared to before optimization.

Figure 7(b) is the spectrum obtained by fast Fourier transform of the electric potential. The fundamental wave content of the optimal ORC-BPMSG is much improved, and the higher harmonics content is much reduced. The *THD* of the optimal ORC-BPMSG is calculated by the formula of *THD*, which is 10.71%, while the *THD* value of the initial prototype model is 19.8%, which is reduced by 45.9%.

This paper compares the performance of the traditional MOPSO with the linear decreasing inertia weight MOPSO and the improved MOPSO. The improved MOPSO is validated using the benchmark function ZDT1. Table 5 shows the comparison of the three MOPSO algorithms in three performance metrics. The generation distance (GD) is an indicator to evaluate the convergence. The spacing (SP) reflects the distribution of the whole solution set in space, and the diversity (DIV) reflects the breadth of

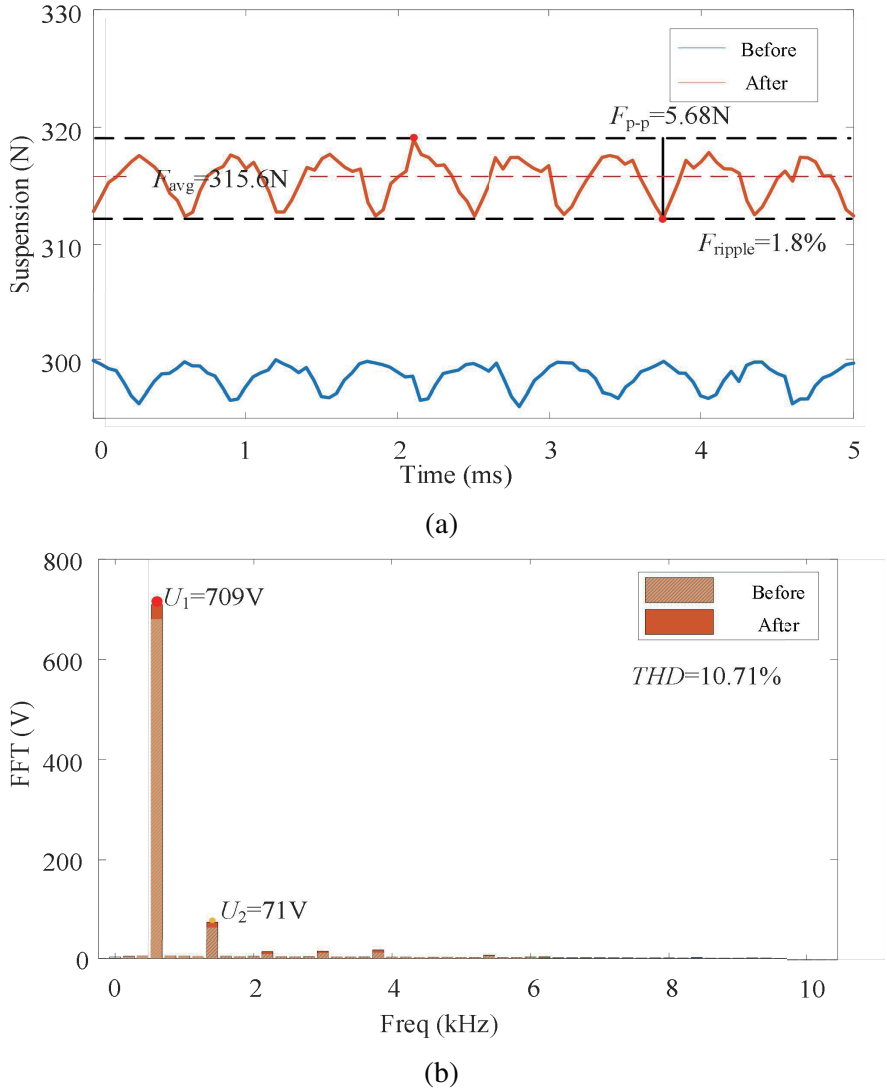

Figure 7. Comparison before and after optimization. (a) Suspension force waveform. (b) FFT frequency spectrum of EMF.

the solution set. For each algorithm, experiments are conducted with the number of particles 50 and the number of iterations 200, and the average value of each metric is calculated by repeating 20 times. The comparison revealed that the GD of the improved MOPSO decreased by 26.25% and the DIV increased by 40.81%, proving that the improved MOPSO has higher convergence accuracy and diversity. Despite the increase of SP by 16.12%, the distribution of the solution set is still more uniform. The above proves that the improved MOPSO has better performance.

Table 5. Comparison of MOPSO algorithms.

Algorithm	GD	SP	DIV
Traditional MOPSO	1.68×10^{-4}	0.45	32.75
Linear decreasing inertia weight MOPSO	1.20×10^{-4}	0.31	53.37
Improved MOPSO	8.85×10^{-5}	0.36	75.15

5. EXPERIMENT RESULTS

The prototype motor is manufactured according to the new motor design parameters obtained after optimization. Figure 8 shows the experimental platform. The generator shown in the experimental

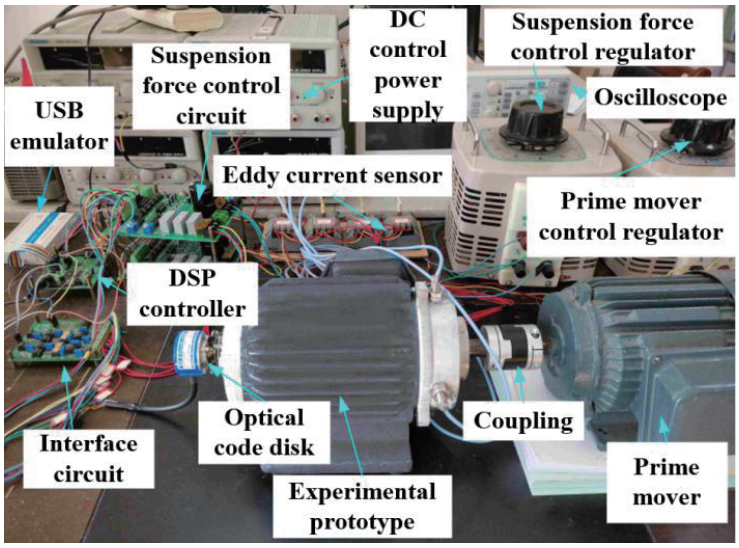

Figure 8. Experimental platform.

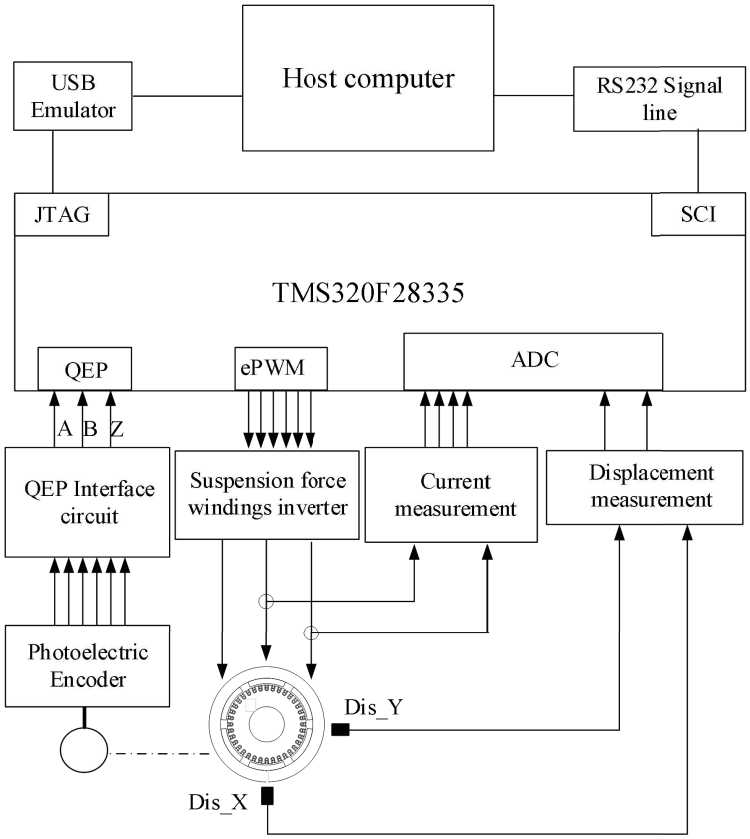

Figure 9. Control diagram of the ORC-BPMSG.

platform is a 36-slot, 6-pole ORC-BPMSG, and the prime mover on the right is an asynchronous motor with a rated speed of 3000 rpm. This experiment needs to verify the *THD* optimization, and the generation of high harmonics is not necessarily related to the generator speed, so the 3000 rpm asynchronous motor is chosen to drive the rotor of the ORC-BPMSG, which can verify the waveform distortion of the generator's electric potential in a safer and more economical scenario. Controllable and stable suspension force is the key to the operation of the ORC-BPMSG. The vibration amplitude of the optimized ORC-BPMSG rotor becomes smaller than the initial prototype under the control of the same control algorithm, then it can be verified that the suspension force pulsation is mitigated.

The system block diagram of the ORC-BPMSG is shown in Figure 9. For the control of the output voltage of the conventional PM synchronous generator, the PWM rectifier module is often added, and the classical control methods used for PM synchronous motors, such as vector control and direct torque control, can be used to control the PWM rectifier module. In order to verify the basic performance of the optimized prototype motor, the prototype motor has no PWM rectifier module added, so only the control schematic of the suspension force winding is available. For the control of the suspension force winding, a TMS320F28335 is used as the processor to generate a controllable PWM signal to control the suspension force control module. The displacement sensor uses an eddy current sensor model Qh8500,

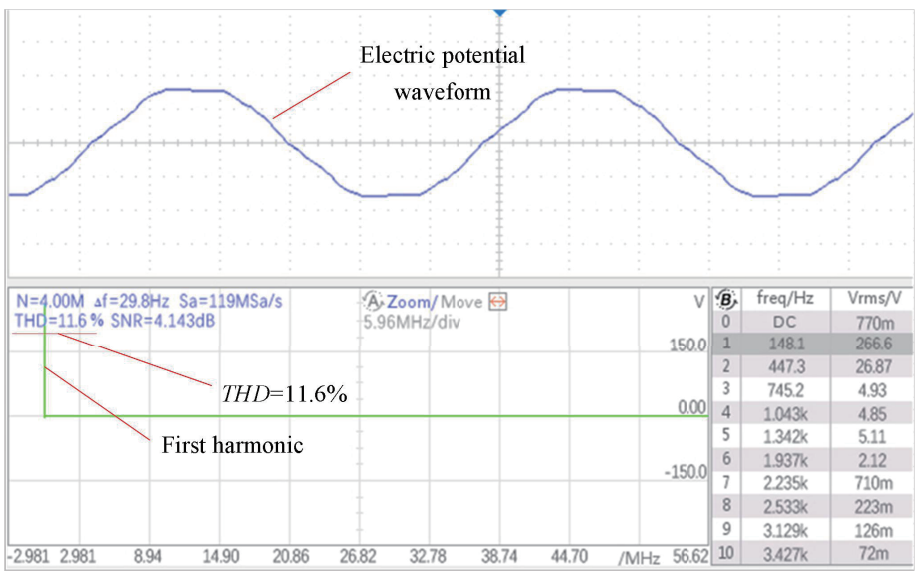

Figure 10. FFT spectrum of oscilloscope.

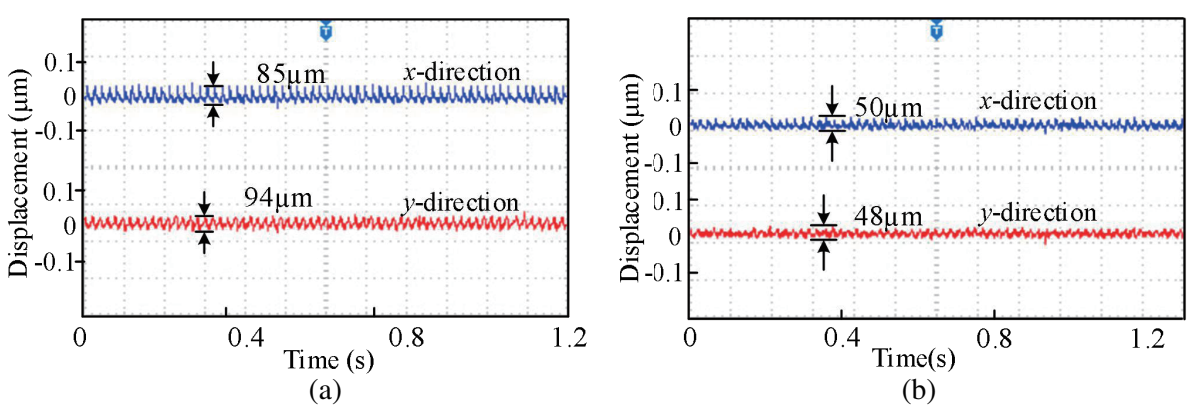

Figure 11. Displacement before and after optimization in x- and y-direction. (a) Radial displacement before optimization. (b) Radial displacement after optimization.

and the relative displacement can be calculated by converting the displacement signal of the rotor off-center into a 0–3 V voltage signal, which is then transmitted to the TMS320F28335. When the rotor is not eccentric, the output voltage is 1.5 V. The experiment needs to suspend the ORC-BPMSG stably, and then use the prime mover to drag the ORC-BPMSG to run.

Figure 10 shows the electric potential waveform and FFT plots generated by the optimized experimental prototype during stable operation with the prime mover dragging at 3000 rpm. It can be seen that the *THD* is 11.6%, which meets the optimization expectation.

Figure 11 shows the rotor displacements in x and y axes before and after optimization. The maximum displacement of the rotor in the x- and y-directions after optimization is changed from 85 μm and 94 μm to 50 μm and 48 μm. It can be obtained that the fluctuations of the force in the x- and y-directions are reduced by 41% and 49%, respectively.

6. CONCLUSION

For the ORC-BPMSG, a multi-objective optimization method based on improved MOPSO is proposed in this paper, which includes establishing the response surface and finding the optimal solution efficiently using improved MOPSO. The optimized ORC-BPMSG is compared with the pre-optimized model using finite element software, and the important indicators of the generator, voltage regulation rate, and total harmonic distortion rate are analyzed in details. The comparison before and after optimization is also performed for the suspension force. From the simulation results, it can be concluded that the performance of the optimized generator has been greatly improved. The optimized harmonic components are less; the harmonic distortion rate is weakened by 45.9%; the average value of the suspension force is also improved by 22%; and the pulsation of the suspension force is lower by 45% than before. Finally, the performance of the optimized ORC-BPMSG is experimentally verified.

ACKNOWLEDGMENT

This work is supported in part by the National Natural Science Foundation of China (61973144), in part by the Priority Academic Program Development of Jiangsu Higher Education Institutions (PAPD-2018-87).

REFERENCES

1. Abdeltawab, H. H. and Y. A. I. Mohamed, "Robust energy management of a hybrid wind and flywheel energy storage system considering flywheel power losses minimization and grid-code constraints," *IEEE Trans. Ind. Electron.*, Vol. 63, No. 7, 4242–4254, Jul. 2016.
2. Zhang, W., H. Yang, L. Cheng, and H. Zhu, "Modeling based on exact segmentation of magnetic field for a centripetal force type-magnetic bearing," *IEEE Trans. Ind. Electron.*, Vol. 67, No. 9, 7691–7701, Sept. 2020.
3. Zhang, W., L. Cheng, and H. Zhu, "Suspension force error source analysis and multidimensional dynamic model for a centripetal force type-magnetic bearing" *IEEE Trans. Ind. Electron*, Vol. 67, No. 9, 7617–7628, Sept. 2020.
4. Zhao, C. and H. Zhu, "Design and analysis of a novel bearingless flux-switching permanent magnet motor," *IEEE Trans. Ind. Electron.*, Vol. 64, No. 8, 6127–6136, Aug. 2017.
5. Zhu, H. and Y. Xu, "Permanent magnet parameter design and performance analysis of bearingless flux switching permanent magnet motor," *IEEE Trans. Ind. Electron.*, Vol. 68, No. 5, 4153–4163, May 2021.
6. Sun, X., L. Chen, and Z. Yang, "Overview of bearingless permanent-magnet synchronous motors," *IEEE Trans. Ind. Electron.*, Vol. 60, No. 12, 5528–5538, Dec. 2013.
7. Zhu, H. and Z. Gu, "Active disturbance rejection control of 5-degree-of-freedom bearingless permanent magnet synchronous motor based on fuzzy neural network inverse system," *ISA Transactions*, Vol. 101, 295–308, Jan. 2020.

8. Steinert, D., I. Kovacevic-Badstübner, T. Nussbaumer, and J. W. Kolar, "Loss investigation of slotless bearingless disk drives," *Proc. IEEE Energy. Convers. Congr. Expo. (ECCE)*, 4418–4424, Sep. 2015.
9. Fu, Y., M. Takemoto, S. Ogasawara, and K. Orikawa, "Investigation of a high speed and high power density bearingless motor with neodymium bonded magnet," *Proc. IEEE Int. Electr. Mach. Driv. Conf. (IEMDC)*, 1–8, May 2017.
10. Sun, Y., B. Su, and X. Sun, "Optimal design and performance analysis for interior composite-rotor bearingless permanent magnet synchronous motors," *IEEE Access*, Vol. 7, 7456–7465, Jan. 2019.
11. Ooshima, M., S. Kitazawa, A. Chiba, and T. Fukao. "Design and analyses of a coreless-stator-type bearingless motor/generator for clean energy generation and storage systems" *IEEE Trans. Magn.*, Vol. 42, No. 10, 3461–3463, Oct. 2006.
12. Ooshima, M., S. Kobayashi, and H. Tanaka. "Magnetic suspension performance of a bearingless motor/generator for flyweel energy storage systems" *IEEE PES Gen. Meet.*, 1–4, Jul. 2010.
13. He, C. and T. Wu, "Analysis and design of surface permanent magnet synchronous motor and generator," *CES Trans. Electr. Mach. Syst.*, Vol. 3, No. 1, 94–100, Mar. 2019.
14. Liu, B., R. Badcock, H. Shu, L. Tan, and J. Fang, "Electromagnetic characteristic analysis and optimization design of a novel HTS coreless induction motor for high-speed operation," *IEEE Trans. Appl. Supercond.*, Vol. 28, No. 4, 1–5, Jun. 2018.
15. Stamenkovic, I., N. Milivojevic, N. Schofield, M. Krishnamurthy, and A. Emadi, "Design, analysis, and optimization of ironless stator permanent magnet machines" *IEEE Trans. Power Electron*, Vol. 28, No. 5, 2527–2538, May 2013.
16. Liu, K., M. Yin, W. Hua, Z. Ma, M. Lin, and Y. Kong, "Design and optimization of an external rotor ironless BLDCM used in a flywheel energy storage system," *IEEE Trans. Magn.*, Vol. 54, No. 11, 1–5, Nov. 2018.
17. Kim, K. and B. Lee, "Taguchi robust design for the multi-response considering the manufacturing tolerance used in high-speed air blower motor," *IET Electr. Power Appl.*, Vol. 14, No. 7, 1141–1147, Feb. 2020.
18. Guo, Y., J. Si, C. Gao, H. Feng, and C. Gan, "Improved fuzzy-based Taguchi method for multi-objective optimization of direct-drive permanent magnet synchronous motors," *IEEE Trans. Magn.*, Vol. 55, No. 6, 1–4, Jun. 2019.
19. Hwang, C., C. Chang and C. Liu, "A fuzzy-based Taguchi method for multiobjective design of PM motors," *IEEE Trans. Magn.*, Vol. 49, No. 5, 2153–2156, May 2013.
20. Zhu, H., S. Shen, and X. Wang, "Multi-objective optimization design of outer rotor coreless bearingless permanent magnet synchronous motor," *IEEE J. Emerg. Sel. Topic Circuits Syst.*, Apr. 2021.
21. Zhang, J., H. Wang, L. Chen, C. Tan, and Y. Wang, "Multi-objective optimal design of bearingless switched reluctance motor based on multi-objective genetic particle swarm optimizer," *IEEE Trans. Magn.* Vol. 54, No. 1, 1–13, Jan. 2018.